Quantitative High Dynamic Range Beam Profiling for Fluorescence Microscopy

T. J. Mitchell,[1, a)] C. D. Saunter,[1] W. O'Nions,[1] J. M. Girkin,[1] and G. D. Love[1]
Centre for Advanced Instrumentation & Biophysical Sciences Institute, Department of Physics, Durham University, Durham DH1 3LE, UK

Modern developmental biology relies on optically-sectioning fluorescence microscope techniques to produce non-destructive *in-vivo* images of developing specimens at high resolution in three dimensions. As optimal performance of these techniques is reliant on the three-dimensional (3-D) intensity profile of the illumination employed, the ability to directly record and analyze these profiles is of great use to the fluorescence microscopist or instrument builder. Though excitation beam profiles can be measured indirectly using a sample of fluorescent beads and recording the emission along the microscope detection path, we demonstrate an alternative approach where a miniature camera sensor is used directly within the illumination beam. Measurements taken using our approach are solely concerned with the illumination optics as the detection optics are not involved. We present a miniature beam profiling device and high dynamic range flux reconstruction algorithm that together are capable of accurately reproducing quantitative 3-D flux maps over a large focal volume. Performance of this beam profiling system is verified within an optical test bench and demonstrated for fluorescence microscopy by profiling the low NA illumination beam of a single plane illumination microscope. The generality and success of this approach showcases a widely-flexible beam amplitude diagnostic tool for use within the life sciences.

I. INTRODUCTION

Fluorescence microscopy is a well-established tool for monitoring the constituent structures within living organisms[1]. The incorporation of fluorescent proteins into genetic structures[2] in conjunction with the development of optical sectioning techniques[3–6] has allowed processes such as embryonic development and cardiac function to be examined at high spatial-temporal resolution in a non-invasive manner[7–11]. The sectioning capability of these techniques is adversely affected by deviation from the optimum illumination point-spread-function (PSF). Indirect profiling of the illumination beam has been performed at high resolution using a suspension of fluorescent beads as a sample in various fluorescence microscopes[12–16] allowing precise engineering of the desired PSF[17,18]. However, these measurements are recorded using the detection optics, and as such couple both the illumination and detection beam paths together in the beam profile.

In this paper we propose and demonstrate a device suitable for profiling the illumination beam of a fluorescence microscope directly that is capable of resolving a wide range of flux over a large volume. We describe an extremely compact waterproof sensor and develop a quantitative high dynamic range (HDR) imaging procedure that overcomes the dynamic range limitations of the sensor; though there has been much work on HDR imaging for photography there has been relatively little on using the technique for quantitative imaging[19,20]. We then present the results of using our combined imaging

procedure and device to profile the illumination beam of an optically-sectioning fluorescence microscope widely adopted for embryonic development studies: a single-plane illumination microscope (SPIM)[21]. Finally, we discuss the limitations of our system and suggest wider future applications of both the device and the HDR imaging procedure.

II. METHODS

A. Instrument Design

A miniature 1 mm × 1 mm footprint 8-bit CMOS sensor, mounted on FlexPCB and optimized for performance in the visible (Awaiba NanEye 2b[22]), was mounted within the compact waterproof housing shown in Fig.1. A glass cover slip of thickness 170 μm, used to seal the sensor within the housing, allowed the device to operate in close proximity to short working distance optical components. To allow 3-D profiling the mounted sensor was affixed to a compact micro-translation stage (Physik Instrument M111.1[23]). The array of the sensor, comprised of 3 μm × 3 μm pitch pixels over a 250 pixel × 250 pixel array, covered an active area of 750 μm × 750 μm. CMOS chip architecture ensured the absence of cross-pixel blooming during exposures where pixel saturation occurs.

———————
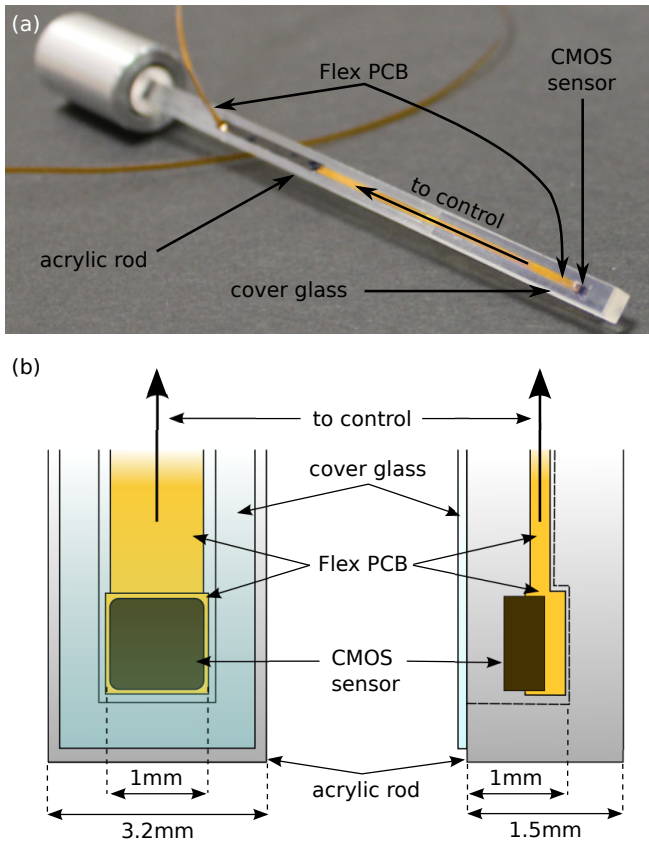a)Electronic mail: t.j.mitchell@dur.ac.uk

FIG. 1. Photograph (a) and schematic (b) of the compact waterproof mounting solution for the Awaiba NanEye 2b CMOS sensor comprising our beam profiling device.

B. HDR Imaging

1. Theory & Calibration

Due to the nature of beam foci, namely the high flux concentrated within the focal volume and the comparatively low flux outside of that, our system was required to resolve a wide range of incident fluxes. Whilst a higher bit-depth sensor could be employed to increase dynamic range, such sensors are currently bulky and do not meet the size constraints placed on the profiling device. As such, we devised a general HDR imaging procedure that could be employed to extend the dynamic range of any sensor. As shown in Fig.2 the standard dynamic range of a sensor operating at a single exposure does not provide adequate sampling of both high and low fluxes. To overcome this limitation a sequential exposure imaging procedure can be implemented that improves the sensitivity of the sensor over an extended flux range; at longer exposures the analog-to-digital unit (ADU) bit-depth of a sensor saturates at lower incident fluxes than those causing saturation at shorter exposures, resulting in the sensor dynamic range providing better low-flux resolution. A simulation of this for an 8-bit sensor is presented in
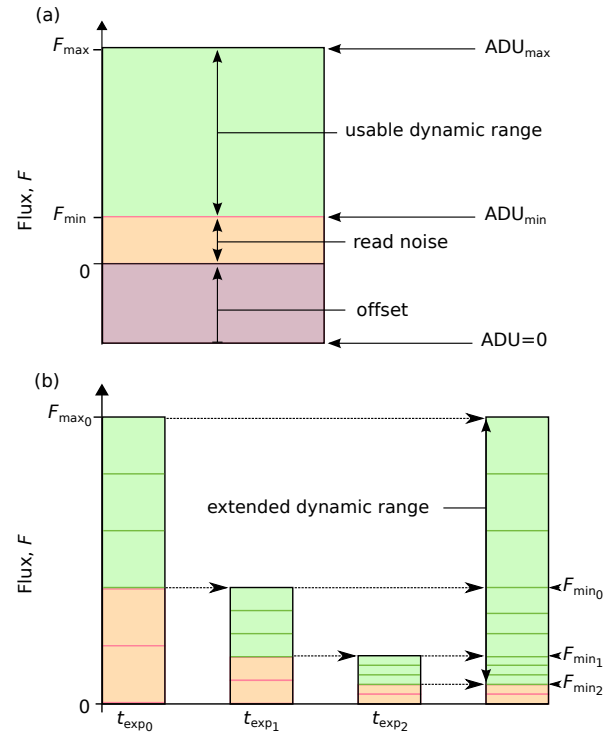

FIG. 2. The dynamic range of a sensor pixel is represented here by a vertical rectangular bar corresponding to the full analog-to-digital unit (ADU) output signal bit-depth (a). The usable region of the dynamic range is affected by offset and read noise, shown as different colored portions of the vertical bar and scaled for emphasis. When a dark image ($F{=}0$) results in an ADU count above zero the ADU headroom has been reduced by the per-pixel offset (purple shading). Above this there is an ADU region that is indistinguishable from the read noise (orange shading) where there is poor resolution between low flux signals. The extent of this region sets the lowest boundary of the usable dynamic range at $\mathrm{ADU_{min}}$, the upper limit of which is set by saturation at $\mathrm{ADU_{max}}$. This usable dynamic range covers a range of incident fluxes that are well-resolved by that sensor pixel for a given exposure. Extension to this range can be achieved through sequential exposure imaging (b). For illustrative purposes the headroom lost due to the offset has been omitted and the range of signals indistinguishable from read noise take up 40% of the total dynamic range. Three successively longer exposures are chosen so that the highest fluxes producing signals lost to read noise are recorded by the usable dynamic range of the next longest exposure. The dynamic range of these three exposures combines to form an extended dynamic range, capable of adequately resolving a wide range of incident fluxes.

Fig.3.

Calibration of our sensor involved taking sequential exposure images of 9 incident fluxes using an integrating sphere (Avantes, AvaSphere-50) to uniformly illuminate the sensor with light of the appropriate wavelength. To roughly match the 488 nm excitation wavelength of
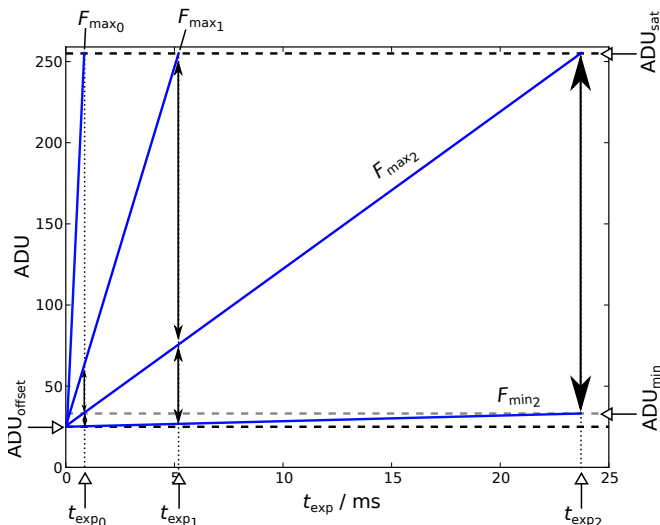
FIG. 3. Demonstration of sequential exposure HDR imaging for a simulated 8-bit sensor pixel exhibiting a linear response to incident flux. The responses to 4 incident flux levels are presented as solid blue lines diverging from a common offset of $\mathrm{ADU_{offset}}$ at $t_{exp} = 0$. Three exposures are noted: t_{exp0}, t_{exp1}, and t_{exp2}. For all exposures the dynamic range of the sensor ranges from $\mathrm{ADU_{offset}}$ up to the saturation signal, $\mathrm{ADU_{sat}}$, shown as horizontal black dashed lines. The presence of read noise, however, dominates low signals and sets a lower limit on the usable dynamic range as the lowest signal distinguishable from read noise, $\mathrm{ADU_{min}}$, presented as a horizontal gray dashed line. Low fluxes that are not well sampled by the dynamic range of the sensor at t_{exp0} can be re-sampled by taking images at longer exposures to improve the signal-to-noise ratio and provide greater distinction between fluxes at the low end. This allows fluxes that were previously indistinguishable from noise to be recovered; fluxes between F_{max2} and F_{min2} that were lost to read noise at t_{exp0} are resolved at t_{exp2}.

many commonly used fluorophores, *e.g.* GFP, a blue LED (wavelength 470 nm, linewidth 10 nm) was used as the calibration light source (note: operation of the profiler at different wavelengths, *e.g.* yellow, green, or red, requires recalibration due to the wavelength dependency of the sensor quantum efficiency). Light from this LED was collected by a plano-convex lens, coupled through a microscope objective lens into the core of a multi-mode fiber, and then fed into the integrating sphere. Prior to the objective lens a filter mount was installed to house a range of absorptive neutral density (ND) filters. The transmission of each ND filter was used as an analog for the relative incident flux, F. For each incident flux, including $F = 1$ where no ND filter was present, images were taken using a range of 14 exposures, linearly spaced between 90 μs and 22.3 ms An offset was applied to the imaging chip to ensure that the dark voltage produced a signal above 0 ADU for all pixels, ensuring no signals were lost at the low end. A gain was also applied to the imaging chip to match the average analogue well saturation level to the maximum output signal of 255 ADU. For each exposure the ADU count for each pixel was taken

as the arithmetic mean of 25 images. The resulting response curves exhibited an atypical flux-dependent offset at low exposures (we attributed this to charge retention in the reset circuitry for the photo-diodes comprising each pixel) that followed a soft-knee transition with increasing exposure into a linear region.

We developed a general equation to describe this non-linear behavior that was then fitted to the response of each pixel. This took the following form:

$$\mathrm{ADU} = C_\alpha \ln(C_\beta F) + \sum_{k=0}^{9} C_k \left(F \times t_{exp}\right)^k, \quad (1)$$

where the $C_{\alpha,\beta,k}$ are free parameters, t_{exp} is the exposure, and F is the relative incident flux. This allowed the relative incident flux to be calculated from a set of sequential exposure images by numerically solving Eqn.1 using the ADU and t_{exp} from an unsaturated exposure to obtain F. To maximize the SNR and obtain the best estimate of the incident flux we selected the longest unsaturated exposure for each pixel. HDR flux profiles were compiled by performing this process for all pixels, as described in Fig.4.

2. Verification

The ability of our procedure to reliably construct HDR flux profiles was verified in a test bench setup. A blue Gaussian laser beam (wavelength 488 nm) was fed through a single-mode fiber, then collimated and passed through an iris aperture, which was in turn demagnified by $3\times$ and focused by a 5 mm diameter achromat lens (Thorlabs AC050-015-A-ML), of focal length of 15 mm, onto the sensor. The iris was used to stop down the beam and enhance the effects of diffraction. A sequence of 10 exposures ranging between 0.2—20 ms were taken, ensuring a sufficient dynamic range overlap between subsequent exposures, and the ADU signal for each exposure was taken from the arithmetic mean of 20 images. Eqn.1 was solved numerically for F using Brent's method[24] using the longest unsaturated exposure of each pixel. Fig.5(a) presents the flux map resulting from our procedure. In Fig.5(b) a typical radial line profile outward from the focus is presented alongside the theoretical Airy diffraction pattern for this setup. The HDR line profile displays strong continuous agreement with theory from a relative incident flux of $F = 5.8$ down to $F \approx 10^{-3}$ where the Airy pattern becomes indistinguishable from noise. Potential improvement to the SNR of our reconstruction at low fluxes is discussed toward the end of the following section.

III. RESULTS & DISCUSSION

Fig.6 shows x-z and y-z sections of a SPIM illumination beam (optical components detailed elsewhere[25]) profiled
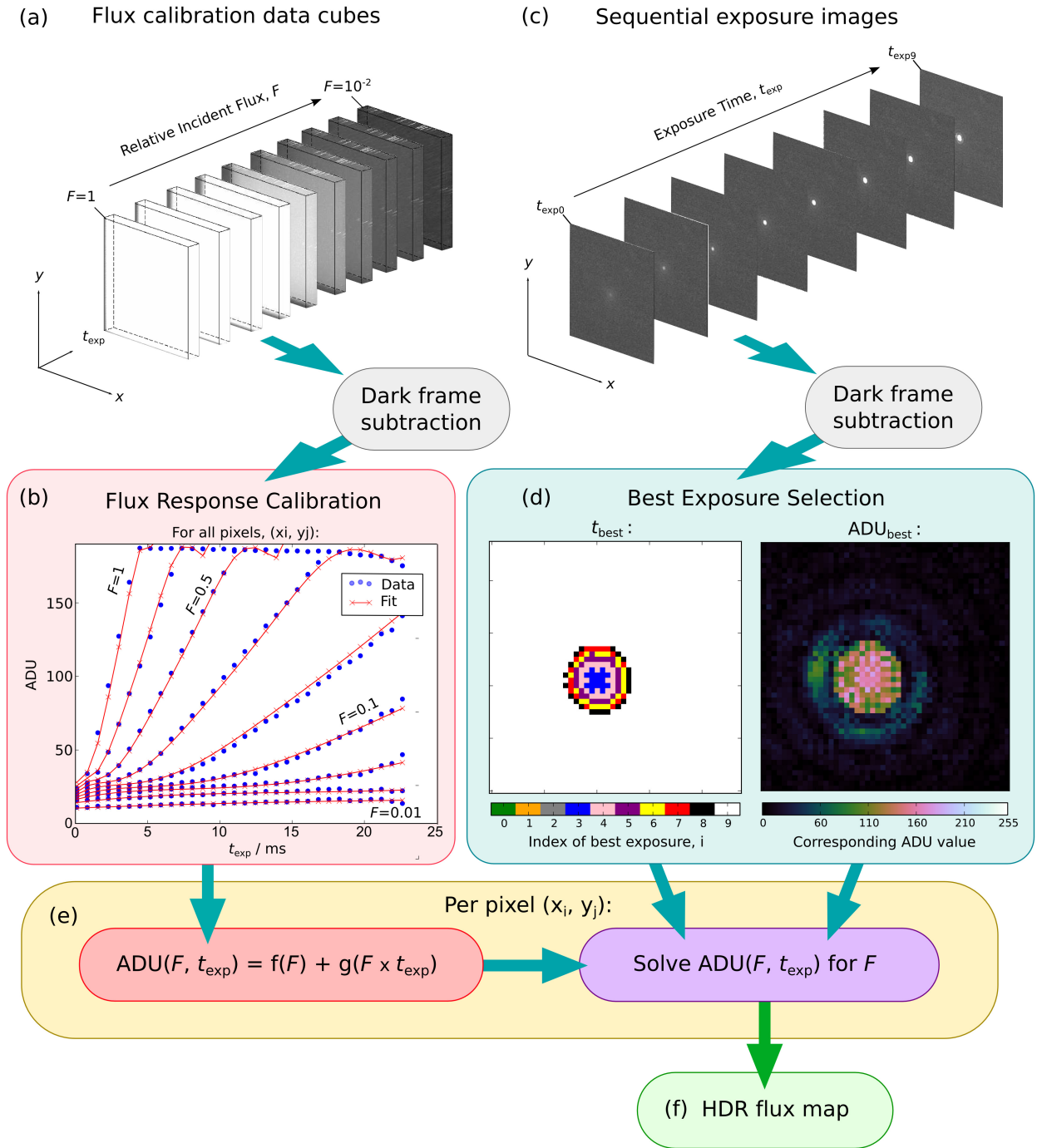
FIG. 4. Flow chart depicting the component processes involved in calibrating our device and composing our HDR flux profiles. Images of uniform illumination are taken over the available range of exposures for a number of different incident fluxes; these form the flux calibration data cubes (a). Following dark frame subtraction a custom polynomial equation is fitted to the calibration data to obtain the time-integrated flux response of each particular pixel. The flux calibration data and fitted response equation are plotted in (b) as blue circles and red curves respectively. Separately, images are taken of the beam of interest using a sequential range of 10 exposures (c); the index of these exposures runs from 0 for the shortest exposure up to 9 for the longest exposure. After dark frame subtraction the longest exposure resulting in an ADU signal below the saturation threshold is selected for each pixel. The leftmost map within box (d) shows the selected index of best exposure, *i.e.* the exposure time index having the highest unsaturated ADU signal, for a central region of the input images. The rightmost map in (d) presents the ADU signals corresponding to the longest unsaturated exposure of each pixel within the same region. The best exposure, t_{best}, and signal, ADU_{best}, are then used to solve the response equation for the best estimate of the incident flux at each pixel, $F(x_i, y_j)$ (e). Once this process has been followed for all pixels the full flux map is compiled (f).
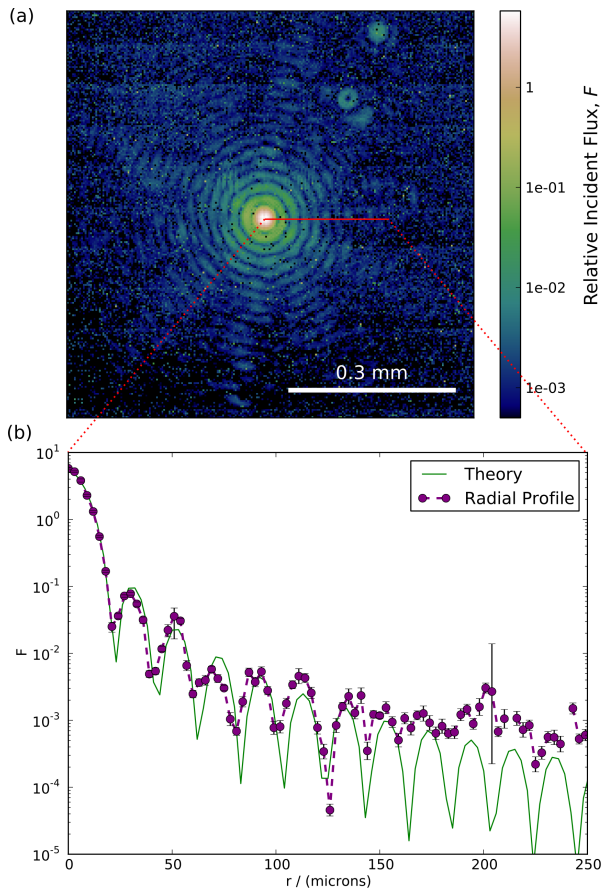
(a)

(b)

FIG. 5. Verification of our procedure by comparing the HDR flux map of a laser beam focus (presented in false-color, (a)) with the theoretical Airy pattern present (b). Logarithmic scales are used for both figures. The radial line profile in (b) demonstrates the capacity of our procedure to resolve a wide and continuous range of fluxes that are several orders of magnitude below the maximum recorded incident flux. Error bars correspond to the standard error on the ADUs used to determine incident flux.

(a)

(b)

FIG. 6. Logarithmic false color x-z (a), and y-z (b) sections through a 3-D HDR flux profile of a SPIM illumination beam within a water tank. The range of flux values have been assigned relative to those used in calibrating the system and are presented on a logarithmic color bar. The x and y scales correspond to pixel coordinates across the sensor; the z scale refers to the coordinates of each slice within the image stack along the optical axis – the closest plane to the focusing lens is at $z = 0$.

by our device. The combined device and translation stage were mounted over the SPIM water tank with the illumination beam (blue laser, wavelength 488 nm) incident on the face of the sensor and images were taken at 90 $z-$ positions over a range of 1 mm along the optical axis of the illumination beam. Our results demonstrate the success of our beam profiler in reconstructing a wide range of fluxes over a volume much larger than the focal region of the beam from a relative magnitude of 10 down to 10^{-3} which allowed us to explore some limitations within our SPIM optical setup. Apparent in both sections are lateral amplitude variations within the beam suggesting that diffraction within the illumination optical train produces a considerable contribution to the beam profile. In addition to this an asymmetric distribution of flux within the beam on either side of the x-z plane focus suggests the illumination beam may not be perfectly aligned to the optical axis of the lenses used. The x-z section also
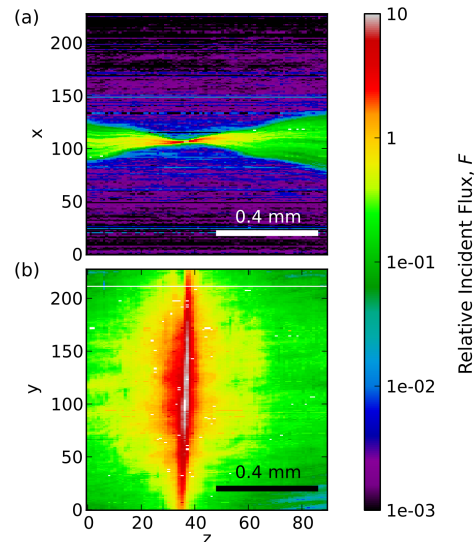
depicts a periodic lateral transit of the beam along z that causes the appearance of this asymmetric distribution to become less clear, though this has been attributed to a lateral motion of the translation stage caused by the rotating leadscrew pitch and has thus been identified as a non-optical effect. The SPIM beam profile showcases a lack of diffraction artifacts outside of the main beam when compared to the test bench beam in Fig.5 since the test bench beam was intentionally devised to test the dynamic range of our HDR imaging procedure. The lateral resolution of our system is limited by the pitch of the sensor array as the focal width of the light sheet fills only one pixel; the focus is therefore not well-resolved as it is sampled below the Nyquist frequency. However, our large-volume direct beam profile could be combined with a complementary small-volume high-resolution indirect profile recorded though the detection optics using sub-resolution fluorescent beads to overcome this limitation. As the HDR imaging procedure could also be implemented separately on the detection camera system, the dynamic range of the fluorescent bead profile could also be extended and a large-volume composite HDR beam profile could be constructed. Alternatively the direct profile resolution could be improved by using a sensor with a smaller pixel pitch, though at the time of writing there appears to be no miniature CMOS sensors commercially available having considerably smaller pixels than those of our chosen sensor; as such the lateral resolution of our

direct beam profiling method is limited by the available technology to the order of around 3 microns.

The system's profiling capabilities could also be improved by implementing two changes: replacement of the translation stage with one exhibiting less lateral motion, and expansion of the sequential imaging procedure through the use of longer exposures. Although the axial resolution of our resulting 3-D reconstruction was intentionally coarse in order to demonstrate the wide range of fluxes across the beam focus that could be reconstructed by our system, there are many higher-precision translation stages that could be used instead. The dynamic range of our reconstruction procedure was limited by the longest exposure available in the camera control software. The use of a wider range of sequential exposures in both imaging and the calibration of the sensor would improve the SNR of low fluxes, providing a much broader beam profiling capability and potentially allowing extremely faint diffraction artifacts to be revealed.

Based on the high quality flux mapping demonstrated in the test bench set up we believe that our system will be of great utility in profiling a variety of beam geometries. As the components of our profiling system are simple and compact, and the calibration and HDR imaging solution presented are general and flexible, we propose that devices similar to ours can be constructed and implemented with ease by those wishing to directly profile beams within any fluorescence microscope system. The ability of our system to record accurate amplitude profiles either side of a beam focus may be well-suited to phase diversity (PD) techniques, such as the Gerchberg-Saxton algorithm, to determine the aberrations present in the illumination beam. PD could also be used to resolve the beam shape at the focus by first calculating the complex field at each intensity plane and then propagating the computed complex waveform of the beam from either input plane to the focal position.

In short, the system is capable of profiling low-power visible-wavelength beams and thus may find alternative applications outside of the microscope, *e.g.* the foci of fiber-coupling assemblies or animal ocular lenses to name just two suggestions.

IV.   SUMMARY

We have developed a HDR beam profiler intended for use within the life sciences and demonstrated its functionality within an optically-sectioning fluorescence microscope. The system hardware is comprised of a miniature 8-bit CMOS sensor embedded within a minimally-invasive waterproof housing. Software has been developed that employs sequential exposure imaging to calibrate the sensor and allow the reconstruction of continuous HDR flux profiles with a dynamic range of over $5 \times 10^3 : 1$. The correctness of this HDR reconstruction procedure has been verified by profiling a low NA beam undergoing broad diffraction and the system has been used to explore the optical limitations of a SPIM. Though the performance of the device is limited by presently available technology, our HDR flux reconstruction procedure is highly general and thus not limited to our specific hardware. The application of our device to fluorescence microscopy can also be extended to allow wavefront determination using PD techniques and may even find use outside of the microscope in determining the optical performance of fiber-coupling assemblies or animal ocular specimens.

[1] B. R. Masters. The Development of Fluorescence Microscopy. In *Encyclopedia Of Life Sciences*, pages 1–9. 2010.

[2] K. G. Peters, P. S. Rao, B. S. Bell, and L. A. Kindman. Green fluorescent fusion proteins: Powerful tools for monitoring protein expression in live zebrafish embryos. *Developmental Biology*, 171(1):252 – 257, 1995.

[3] M. A. A. Neil, R. Juskaitis, and T. Wilson. Method of obtaining optical sectioning by using structured light in a conventional microscope. *Opt. Lett.*, 22(24):1905–1907, December 1997.

[4] J. A. Conchello and J. W. Lichtman. Optical sectioning microscopy. *Nature methods*, 2:920–931, 2005.

[5] P. A. Santi. Light sheet fluorescence microscopy: a review. *The Journal of Histochemistry and Cytochemistry: Official Journal of The Histochemistry Society*, 59(2):129–38, February 2011.

[6] J. Mertz. Optical sectioning microscopy with planar or structured illumination. *Nature Methods*, 8(10):811–819, September 2011.

[7] M. Mavrakis, R. Rikhy, M. Lilly, and J. Lippincott-Schwartz. Fluorescence imaging techniques for studying Drosophila embryo development. *Current protocols in cell biology*, Chapter 4:4.18, 2008.

[8] M. Weber and J. Huisken. Light sheet microscopy for real-time developmental biology. *Current opinion in genetics & development*, 21(5):566–72, October 2011.

[9] R. Tomer, K. Khairy, and P. J. Keller. Shedding light on the system: studying embryonic development with light sheet microscopy. *Current opinion in genetics & development*, 21(5):558–65, October 2011.

[10] P. J. Keller. In vivo imaging of zebrafish embryogenesis. *Methods (San Diego, Calif.)*, 62(3):268–78, August 2013.

[11] J. M. Taylor, J. M. Girkin, and G. D. Love. High-resolution 3D optical microscopy inside the beating zebrafish heart using prospective optical gating. *Biomedical optics express*, 3(12):3043–53, December 2012.

[12] P. J. Shaw and D. J. Rawlins. The point-spread function of a confocal microscope: its measurement and use in deconvolution of 3-D data. *Journal of Microscopy*, 163(2):151–165, 1991.

[13] H. Yoo, I. Song, and D. G. Gweon. Measurement and restoration of the point spread function of fluorescence confocal microscopy. *Journal of Microscopy*, 221:172–176, 2006.

[14] M. J. Nasse, J. C. Woehl, and S. Huant. High-resolution mapping of the three-dimensional point spread function in the near-focus

region of a confocal microscope. *Applied Physics Letters*, 90, 2007.

[15] R. W. Cole, T. Jinadasa, and C. M. Brown. Measuring and interpreting point spread functions to determine confocal microscope resolution and ensure quality control. *Nature protocols*, 6:1929–41, 2011.

[16] C. J. Engelbrecht and E. H. Stelzer. Resolution enhancement in a light-sheet-based microscope (SPIM). *Optics Letters*, 31(10):1477–1479, 2006.

[17] M. Martínez-Corral. Point spread function engineering in confocal scanning microscopy. *Wave-Optical Systems Engineering II*, 5182:112–122, 2003.

[18] M. A. Neil, R. Juskaitis, T. Wilson, Z. J. Laczik, and V. Sarafis. Optimized pupil-plane filters for confocal microscope point-spread function engineering. *Optics letters*, 25:245–247, 2000.

[19] S.K. Nayar and T. Mitsunaga. High dynamic range imaging: spatially varying pixel exposures. *Proceedings IEEE Conference on Computer Vision and Pattern Recognition. CVPR 2000 (Cat. No.PR00662)*, 1:472–479, 2000.

[20] P. E. Debevec and J. Malik. Recovering High Dynamic Range Radiance Maps from Photographs. In *ACM SIGGRAPH 2008 Classes*, SIGGRAPH '08, pages 31:1—-31:10, New York, NY, USA, 2008. ACM.

[21] K. Greger, J. Swoger, and E. H. K. Stelzer. Basic building units and properties of a fluorescence single plane illumination microscope. *Review of Scientific Instruments*, 78(2):023705, 2007.

[22] M. Wäny and S. Voltz. Awaiba NanEye Camera System specifications. `http://www.awaiba.com/v2/wp-content/uploads/2010/01/NanEye_Camera_system_Spec_v_1.06.pdf`. Accessed: 2014-06-29.

[23] Gmbh & Co. KG. Physik instrument Compact Micro-Translation Stage specifications. `http://www.physikinstrumente.com/en/pdf/M110_Datasheet.pdf`. Accessed:2014-06-29.

[24] G. E. Forsythe, M. A. Malcolm, and C. B. Moler. In *Computer Methods for Mathematical Computations*, chapter 7.2. Prentice-Hall, Englewood Cliffs, NJ, 1977.

[25] C. Bourgenot, C. D. Saunter, J. M. Taylor, J. M. Girkin, and G. D. Love. 3D adaptive optics in a light sheet microscope. *Optics Express*, 20(12):13252, May 2012.